Early Postseismic Deformation of the 29 July 2021 Mw8.2 Chignik Earthquake Provides New Constraints on the Downdip Coseismic Slip

Zechao Zhuo[1], Jeffrey Todd Freymueller[1], Zhuohui Xiao[2], Julie Elliott[1], and Ronni Grapenthin[3]

[1]Michigan State University
[2]Wuhan University
[3]University of Alaska Fairbanks

July 20, 2023

Abstract

On 29 July 2021, an Mw 8.2 megathrust earthquake struck the Alaska Peninsula. Quantifying the coseismic slip and the afterslip that followed this earthquake provides us the opportunity to clarify the megathrust slip budget and the earthquake hazard potential there. However, the estimated coseismic slip distribution inversion result is strongly affected by assumptions made in the inversion. The spatial pattern of stress-driven afterslip is mainly controlled by the coseismic slip distribution, so that it can provide new information about the coseismic slip distribution and is useful to assess the assumptions made in the coseismic inversion. The orientation and relative magnitudes of postseismic displacements at sites on the Alaska Peninsula require that the afterslip be concentrated ~130km from the trench. As a result, coseismic slip models including slip at that distance or less to shore, predict postseismic deformation that systematically misfits the observations. A narrower coseismic rupture plane with an abrupt downward termination of slip provides a much better fit to the observed postseismic signal than models where the slip tapers gently with depth. We considered multiple different viscoelastic relaxation models and find that these conclusions about the coseismic model are required regardless of the viscoelastic relaxation models used. The contribution of viscoelastic relaxation to the observed signal is not negligible, and the early postseismic observations are best reproduced with a model that features a 50 km thick elastic lithosphere for the overriding plate, and an elastic cold nose to the mantle wedge.

Hosted file

968567_0_art_file_11188054_rxr5jb.docx available at https://authorea.com/users/639054/articles/655453-early-postseismic-deformation-of-the-29-july-2021-mw8-2-chignik-earthquake-provides-new-constraints-on-the-downdip-coseismic-slip

Hosted file

968567_0_supp_11188093_rxr636.docx available at https://authorea.com/users/639054/articles/655453-early-postseismic-deformation-of-the-29-july-2021-mw8-2-chignik-earthquake-provides-new-constraints-on-the-downdip-coseismic-slip

Early Postseismic Deformation of the 29 July 2021 Mw8.2 Chignik Earthquake Provides New Constraints on the Downdip Coseismic Slip

Z. Zhuo[1], J.T. Freymueller[1], Z. Xiao[2], J. Elliott[1], and R. Grapenthin[3]

[1]Michigan State University

[2]Kunming University of Science and Technology

[3]University of Alaska Fairbanks

Corresponding author: Zechao Zhuo(zhuozech@msu.edu)

Key Points:

- The spatial pattern of afterslip provides new information about the coseismic slip distribution of the 2021 Mw8.2 Chignik earthquake.
- Displacements due to viscoelastic effects depend strongly on the viscosity model, but are insensitive to the details of the coseismic slip.
- The maximum depth of the Chignik coseismic rupture constrained by the stress-driven afterslip is about 35km based on the Slab2.0 geometry.

Abstract

On 29 July 2021, an Mw 8.2 megathrust earthquake struck the Alaska Peninsula. Quantifying the coseismic slip and the afterslip that followed this earthquake provides us the opportunity to clarify the megathrust slip budget and the earthquake hazard potential there. However, the estimated coseismic slip distribution inversion result is strongly affected by assumptions made in the inversion. The spatial pattern of stress-driven afterslip is mainly controlled by the coseismic slip distribution, so that it can provide new information about the coseismic slip distribution and is useful to assess the assumptions made in the coseismic inversion. The orientation and relative magnitudes of postseismic displacements at sites on the Alaska Peninsula require that the afterslip be concentrated ~130km from the trench. As a result, coseismic slip models including slip at that distance or less to shore, predict postseismic deformation that systematically misfits the observations. A narrower coseismic rupture plane with an abrupt downward termination of slip provides a much better fit to the observed postseismic signal than models where the slip tapers gently with depth. We considered multiple different viscoelastic relaxation models and find that these conclusions about the coseismic model are required regardless of the viscoelastic relaxation models used. The contribution of viscoelastic relaxation to the observed signal is not negligible, and the early postseismic observations are best reproduced with a model that features a 50 km thick elastic lithosphere for the overriding plate, and an elastic cold nose to the mantle wedge.

Plain Language Summary

Determining where and how much slip occurs during an earthquake allows us to estimate the remaining earthquake hazard potential. Models of earthquake slip can vary from each other a lot when the data are sparse, because of assumptions such as the geometry and spatial extent of the rupture plane and the roughness of the slip distribution. The early postseismic process is dominated by afterslip on the rupture plane, which is sensitive to the slip distribution of the coseismic event, under the model of stress-driven afterslip. Postseismic GPS displacements are a completely different dataset from the coseismic observations, and provide new and independent information about the earthquake rupture. We test how a range of coseismic slip models for the July 29, 2021 Mw8.2 Chignik earthquake, all of which can fit the coseismic data well, predict postseismic deformation over three months and compare that with GPS measurements. We find that the postseismic data provides a good constraint on the spatial distribution of coseismic slip, especially at the downdip (deeper) end of the rupture. A more spatially compact coseismic rupture is required to generate the stress-driven afterslip that can fit the data, no matter what viscoelastic relaxation contribution considered.

1 Introduction

The Alaska-Aleutian subduction zone has hosted several great megathrust earthquakes in the last century, including the 1938 Mw8.2, 1946 Mw8.6, 1957 Mw8.6, 1964 Mw9.2 and 1965 Mw8.7 earthquakes (Nishenko and Jacob, 1990). Recently, the Mw7.8 Simeonof earthquake (e.g., Xiao et al., 2021 struck the Shumagin islands on July 21, 2020 followed by the Mw 7.6 strike-slip Sand Point earthquake on October 19. On July 29, 2021 — advanced by the Simeonof earthquake — the Mw8.2 Chignik earthquake (Elliott et al., 2022) struck the adjacent Semidi segment, to the NE of the 2020 Mw7.8 event. The Chignik earthquake partially re-ruptured the

1938 Mw8.2 coseismic rupture zone (Figure 1). The availability of multiple forms of geodetic and seismic data provides us with a great opportunity to fully assess the coseismic slip and the post-seismic processes that followed, helping us to quantify the slip budget and earthquake potential of this section of the Alaska-Aleutian subduction zone.

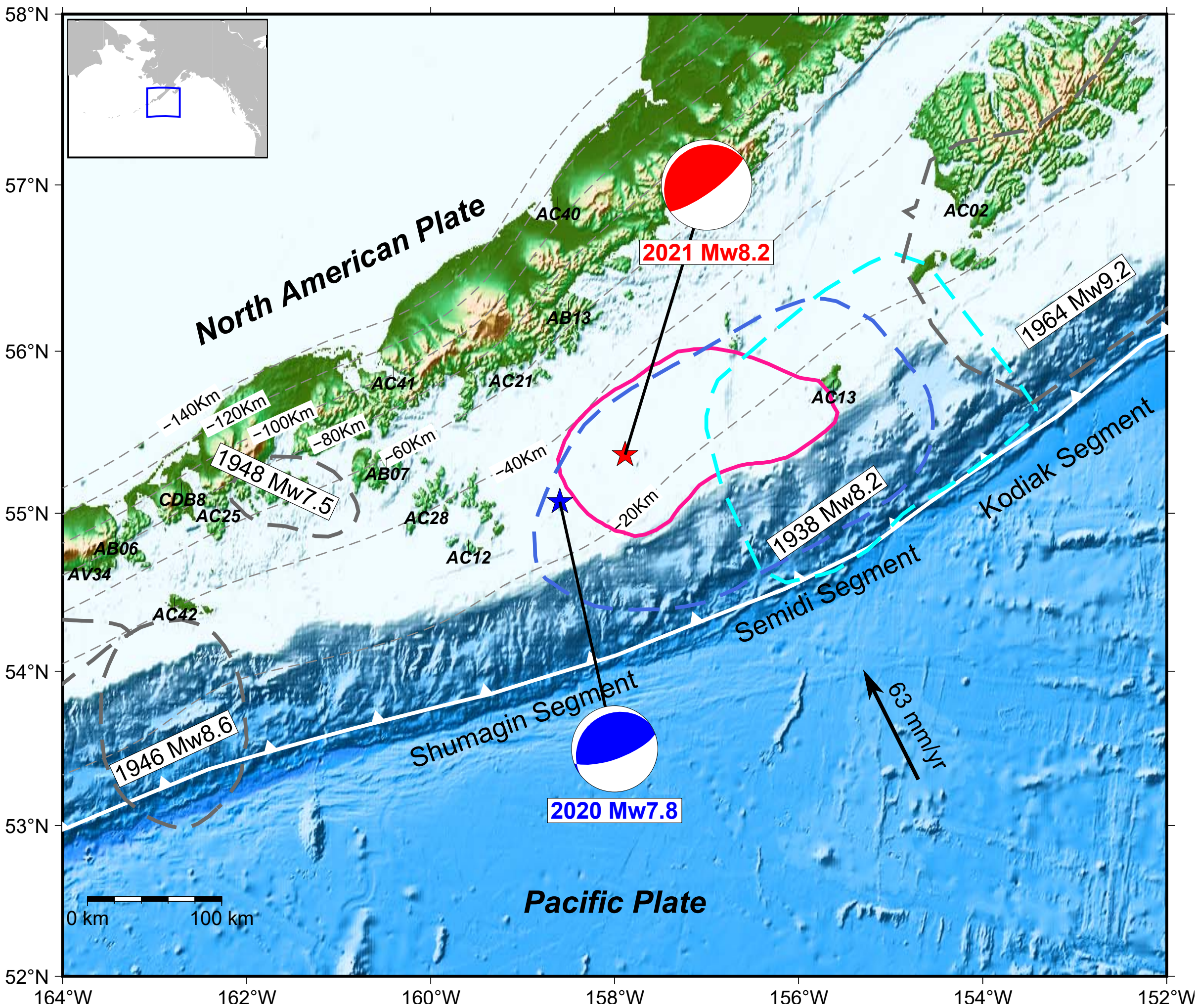

Figure 1. Tectonic setting of the Alaska-Aleutian subduction zone. The gray shaded patches with dashed lines indicate the historical rupture regions. The light blue dashed line shows the tsunami source model of the 1938 Mw8.2 earthquake determined by Freymueller et al. (2021). The blue dashed line show an alternative rupture area of the 1938 Mw8.2 earthquake. The blue and red shadowed region indicate the coseismic rupture areas of the 2020 Mw7.8 Simeonof event (Xiao et al., 2022) and 2021 Mw 8.2 Chignik event, respectively. The two stars and two beach balls indicate the epicenters and GCMT solutions of the 2020 event (blue) and 2021 event (red), respectively. The orange cycles scaled by magnitude show the 30-day aftershocks following the 2021 event. The red cycles show the location of the GPS continue sites used in this study. Dashed light grey lines outlines the depth contours from the Slab2 model (Hayes et al., 2018). The white barbed line shows the plate boundary between the Pacific plate and the North American plate. The black arrow shows the Pacific plate velocity relative to the North American plate (DeMets et al., 2010).

Several coseismic rupture models have been published for the July 29, 2021, Mw8.2 Chignik earthquake (Elliott et al., 2022; Ye at al., 2022; Liu et al.,2022; Mulia et al., 2022), using different inversion assumptions and regularization methods, and slightly different coseismic observation data sets. Therefore, it is difficult to determine which coseismic model better recovers the actual slip distribution by using the coseismic observations only. Ye et al. (2022) argued that their model better resolves the up-dip portion of the coseismic slip distribution because they added tsunami data as an additional constraint, but for the down-dip portion of the coseismic rupture, each published model seems to do equally well in terms of fitting the coseismic observations. Despite the similarity in fit, the shape of the slip distributions of those models vary considerably at the down-dip end (Figure 2).

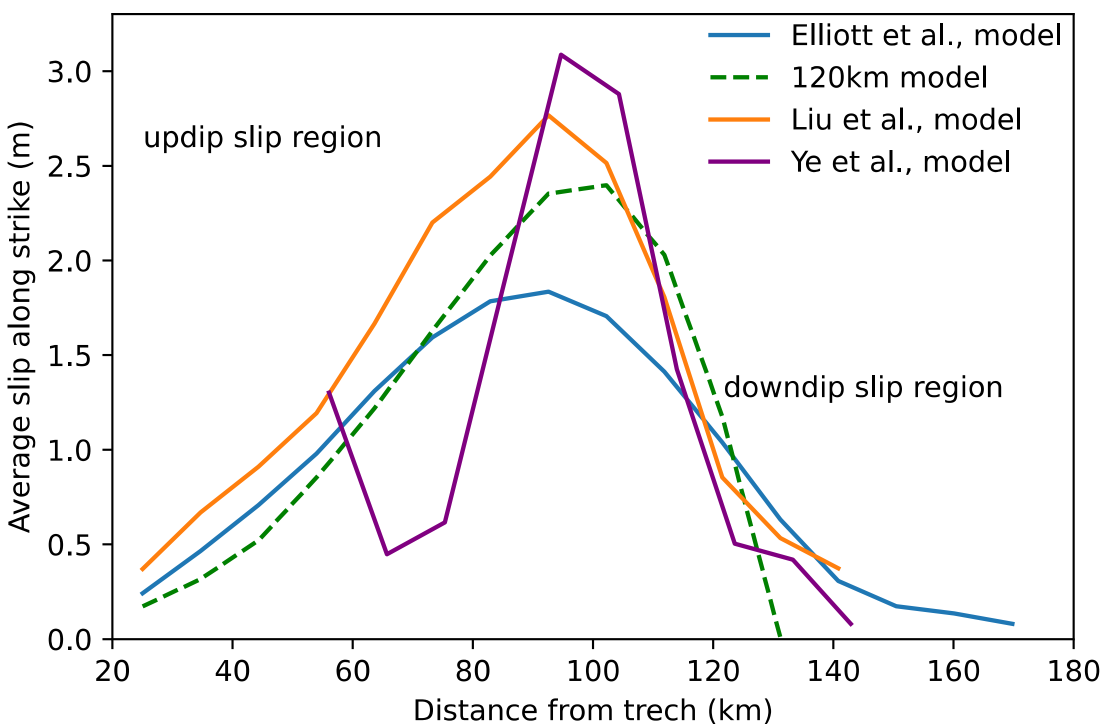

Figure 2. Average slip along strike of different existing coseismic models. Solid lines show the average coseismic slip along strike of published models, dashed line show the average coseismic slip along strike of our preferred coseismic model with 120km fault width.

Stress-driven afterslip provides a physically based model for post-seismic afterslip (Wang and Fialko, 2018). In this kind of model, the slip distribution and time history of afterslip is determined by the coseismic slip and the frictional properties of the fault plane. Under the assumption of frictional homogeneity on the fault plane, the spatial pattern of the stress-driven afterslip is determined entirely by the coseismic slip distribution, while the frictional parameters control the time evolution of slip and displacement.

In this study, we first compare the stress-driven afterslip predictions for three published slip models for the 2021 Chignik earthquake (Elliottet al., 2022; Liu et al., 2022; Ye et al., 2022), and find that most of the models show significant misfit to the postseismic displacements (section 4.1). We find that the azimuthal misfits in some models result from the peak afterslip being located too close to the coastline; the location of the peak afterslip is determined mainly by the downdip end of the slip distribution. Using the insights gained from these comparisons, we then systematically vary the coseismic slip inversion to identify how the coseismic slip model must change to best predict the afterslip, considering a range of models for the contribution of viscoelastic relaxation. Finally, as an additional test of our conclusions about the slip model, we compare the model predictions to the data from GPS campaign measurements collected three weeks after the earthquake, which contain both coseismic and postseismic signal contributions.

2 Data

2.1 Data Used to Estimate the Coseismic Slip Distribution

We used the same coseismic data set as Elliott et al. (2022), along with the same inversion approach, and more details of the data processing and preparation are given there. We used static coseismic offsets in the ITRF2014 reference frame computed from the daily GNSS time series, processed with the GIPSY-OASIS gos-6.4 software (Zumberge et al., 1997; Bertiger et al., 2020). InSAR displacements, processed with GMTSAR (Sandwell et al., 2011), were included, and tied to GNSS sites where possible to provide absolute line-of-sight displacements. We included high rate GNSS, teleseismic broadband, and near-source strong-motion waveforms in the joint inversion. The 1 sps high-rate GPS time series were generated with GipsyX (Bertiger et al., 2020) and filtered with a 0.4 Hz cut-off frequency to suppress noise. In addition, 46 P and 22 SH global tele-seismic waveforms were included in the inversion as well to improve observation geometry. The raw tele-seismic waveforms were integrated into ground displacements after bandpass filtering between 0.01 ~ 1 Hz.

2.2 Data Used to Study the First Three Months of Post Seismic Deformation at Continuous GPS Sites

We used data from the continuous GPS sites along the Alaska subduction zone to estimate the displacements due to the first three months of post-seismic deformation. We fit a parametric model to each site's time series to isolate the postseismic displacements from the interseismic, coseismic and seasonal deformation. We fit the model to the time series starting from January

2018 after the M7.8 earthquake in the Gulf of Alaska (Ruppert et al., 2018) and ending at 3.3 months after the Chignik earthquake. The surface displacements of the sites we study due to the November 30, 2018 Mw7.1 Anchorage earthquake are very small, and were not corrected or considered in our analysis. The model includes terms for the linear interseismic velocity, annual and semi-annual seasonal displacements, and time dependent terms for the Simeonof, Sand Point, and Chignik earthquakes. For the Simeonof earthquake, we estimated the coseismic offset plus a logarithmic relaxation with a relaxation time of 0.025 years to account for the postseismic deformation. For the Sand Point earthquake, we estimated the coseismic displacement only, as there is no evidence for a measurable postseismic transient (including such a term does not change other model parameter values or improve the fit). For the Chignik earthquake, we estimated the coseismic displacements plus a logarithmic relaxation with a relaxation time of 0.005 years to account for the postseismic deformation.

We compute the postseismic displacements for Chignik by evaluating only the term for the post-Chignik relaxation at two different epochs, three weeks and three months after the earthquake. The vertical data were not used in our primary models because it has a relatively small signal, larger noise, and it is more difficult to model time-varying displacements caused by seasonal loading, glacial isostatic adjustment and other signals. However, we did explore how postseismic models fit the vertical data.

2.3 Campaign GPS Data

We also utilize campaign GPS data collected three weeks after the Chignik earthquake, at survey marks that had long-term pre-earthquake interseismic campaign measurements (Li and Freymueller, 2018). Eight sites in the near field of the Chignik rupture were surveyed as part of the Chignik earthquake repid respond activity from 08/17/2021 – 08/25/2021. These data were analyzed using the same methods as the continuous site data to estimate daily positions. We estimated displacemements that combine the coseismic displacement and 3 weeks of posteismc displacement by fitting a model that included the pre-earthquake trend and an offset at the time of the earthquake.

3 Methods

3.1 Coseismic Slip Inversions

We estimated the coseismic slip model using exactly the same data and method used by Elliott et al. (2022), except for the variations in the fault plane as noted below. The details of the inversion technique, which is based on the method of Ji et al. (2002). are described by Xiao et al. (2021). The epicenter of this event was taken from the U.S. Geological Survey (USGS) estimate, and we pinned its depth (26.2 km) to the slab depth as estimated by Slab2.0. The model fault plane is a local average of the Slab2.0 geometry which has a strike angle of 235° and a dip angle of 15°. All of the fault planes have an along-strike length of 320km, and the downdip widths of the fault vary from 100km to 160km. The subfaults are all 10km by 10km squares, and we imposed zero slip conditions around all edges of the model plane; this affects the structure of the Laplacian smoothing operator at the fault edges. For the bottom edge, we also specifically imposed zero slip on the deepest row of subfaults. As a result, the effective wdith of the slip model is 10 km smaller than the width of the plane, and we identify models by this smaller effective width where slip is allowed to happen.

The fault model plane used by Elliott et al. (2022) had a total width of 160km, which extended well beyond the likely maximum depth of the coseismic rupture so that edge effects from the zero slip condition would not affect the estimated model. In this study, we repeat the slip inversion assuming alternate definitions of the fault plane, varying either the geometry (depth, dip angle) or the spatial extent of the model fault plane.

3.2 Modeling of Post-seismic Deformation

Post-seismic deformation includes afterslip on the fault interface, viscoelastic relaxation of the surrounding material, and poroelastic rebound due to fluid flow driven by pressure changes due to the coseismic rupture. Hu et al. (2014) studied the poroelastic rebound contribution following the 2011 Tohoku earthquake and found that the poroelastic rebound contribution to surface deformation is mainly limited to the vicinity of the rupture area. In our case, we only have one GPS continuous site (AC13) that is located at the updip end of the coseismic rupture zone. Thus, here we only take afterslip and viscoelastic relaxation into consideration. We model stress driven afterslip and include a 2.5D model for viscoelastic relaxation.

3.2.1 Stress-driven Afterslip Simulation

We carried out stress-driven afterslip simulations using the open-source software RELAX, which solves for the nonlinear time-dependent slip on the fault *s*(*x*,*t*) in the Fourier domain under the assumption of rate-strengthening friction on faults (equation 1) (Barbot et al., 2009a). The afterslip evolution history on a given patch of the fault is controlled by the rate-strengthening constitutive law (Barbot et al., 2009a).

$$s(t) = \frac{\Delta\tau_0}{G^*}\left[1 - \frac{2}{k} coth^{-1}\left(e^{\frac{t}{t_0}} coth\, coth\, \frac{k}{2}\right)\right] \quad (1)$$

In equation 1, $k = \frac{\Delta\tau_0}{a\sigma}$ is the dimensionless ratio that controls the nonlinearity during the slip, and the time evolution is controlled by *k* along with the relaxation time $t_0 = \frac{1}{2V_0}\frac{a\sigma}{G^*}$. Note that the parameter *a* in the equations of Barbot et al. (2009), and as used here, is more commonly identified as (*a*-*b*) in the context of full rate and state friction. Larger values of *k* result in models that are more strongly non-linear, with a more rapid decay in slip velocity early in the postseismic period (these models also require shorter model time steps and thus result in much longer program execution time). $\Delta\tau_0$ refers to the shear stress perturbation due to the earthquake, σ refers to the effective normal stress on the fault, and G* is the effective elastic constant per unit area determined by the linear dimension L and the shear modulus. The relaxation time $t_0 = \frac{1}{2V_0}\frac{a\sigma}{G^*}$ depends on both aσ and the reference sliding velocity on the fault V_0. Total slip as *t* goes to infinity is limited to $\frac{\Delta\tau_0}{G^*}$.

Thus, there are 2 unknown parameters to search for to solve this problem: $a\sigma$ and V_0. Many studies assume a value of $a\sigma$ and search only for V_0, due to the strong parameter tradeoff between the two values when only one time period is considered (e.g., Tian et al., 2020). We first performed a 2-d grid search for $a\sigma$ and V_0 over a relatively large range of parameter values to find the best fit values. We calculated the reduced χ^2 using the three sites on the Alaska Peninsula (AC40, AB13 and AB21, see Figure 1) that are most sensitive to the downdip afterslip.

When we consider only one time interval, for example three months, then a very wide range of $a\sigma$ values, varying by orders of magnitude, yields models that fit the data equally well. Large values of $a\sigma$ (such as 3MPa suggested by Tian et al. (2020)) produce an afterslip evolution history at GPS sites like the orange curve in Figure 3, showing a low degree of nonlinearity, while small values of $a\sigma$ (similar to those used by Wang and Bürgmann (2020) or Zhao et al. (2022)) produce models like the blue curve in Figure 3, showing a higher degree of nonlinearity. Because the observations at 3 weeks more closely align with the curve produced by smaller values for $a\sigma$ (Figure 3 gray star), we limit the range of parameter values to those similar to those of Zhao et al. (2022) and consider displacement predictions for two time windows, 0-3 weeks after the mainshock and 0-3 months after. Based on the total misfit and given the nonlinear nature of the very early afterslip evolution, we fix the value of $a\sigma$ to be 0.6 MPa. Given that the two time windows we have used are short, using a different value of $a\sigma$ in our models would produce an equally good fit, with a correspondingly different V_0 value. In this study, we vary the V_0 value for each different model scenario that we consider in the following sections, and we leave the question of whether it is possible to determine an optimal value of $a\sigma$ to a future study with a longer time span.

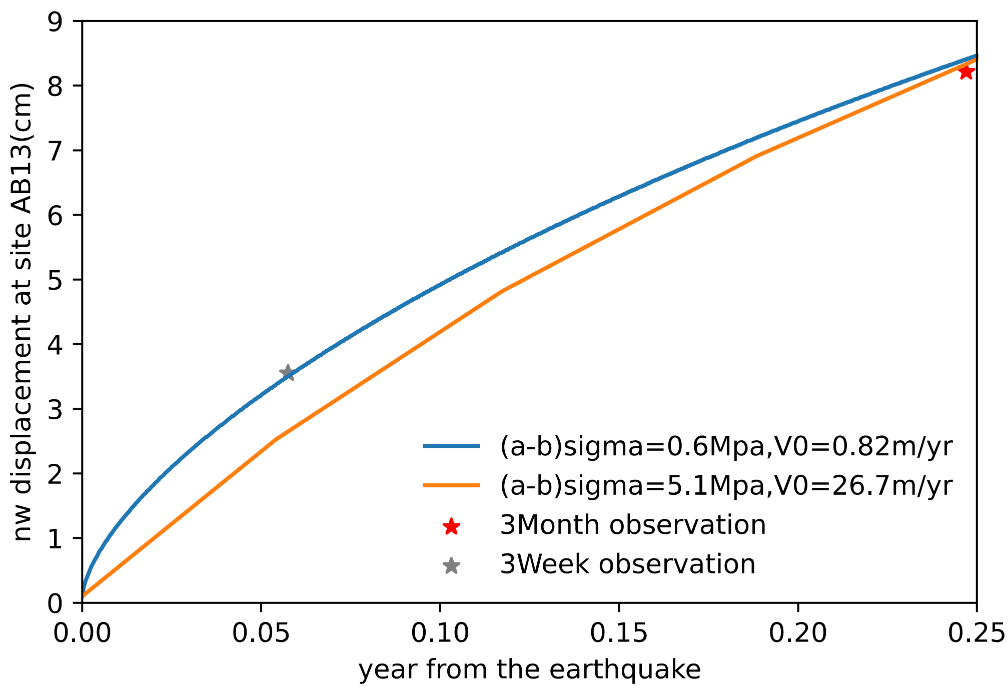

Figure 3. prediction of NS displacement at site AB13 using 2 combos of a-b sigma and V0. Blue and orange curve indicates the NS displacement evolution history calculated by RELAX. Red and grey stars show the observation at 3 week and 3 months, respectively.

3.2.2 Viscoelastic Relaxation Simulation

Although afterslip is likely to be the dominant process in the early period of the post-seismic deformation, for an Mw8.2 event it is necessary to consider the viscoelastic contribution to the observed post-seismic signal as well (Sun and Wang, 2015). However, it is known to be difficult to separate the two post-seismic processes in the early time period (Sun and Wang, 2015).

Therefore, we consider a range of viscoelastic relaxation models based on different assumed viscoelastic structures, subtract these from the data, and then estimate the best-fitting afterslip model for each case.

The numerical simulation we use is the software package VISCO2.5D, which imposes source and domain boundary conditions on a 2-D structure to approximate the 3-D equations of quasi-static equilibrium by the spectral element method (Pollitz, 2014). We use the Slab2.0 slab geometry at the center of the coseismic rupture and assume a laterally homogeneous viscosity structure (Figure 4a, b). The elastic slab separates the sub-oceanic asthenosphere from the mantle wedge. We vary the viscosity in the mantle wedge, and include a 90km thick elastic slab (including its mantle lithosphere). We also varied the continental lithosphere thickness and the presence of a cold nose to the mantle wedge (e.g., Luo and Wang, (2021)). All of these model assumptions affect our model predictions (see section 4.2).

(a) (b)

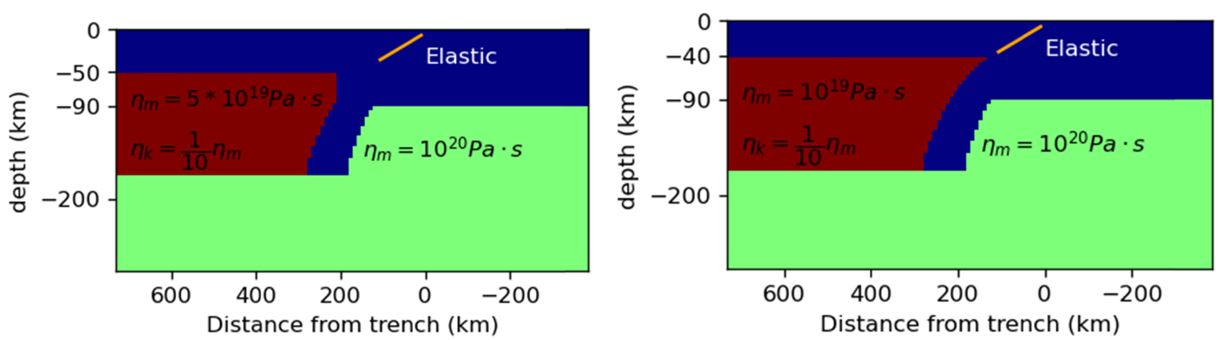

(c) (d)

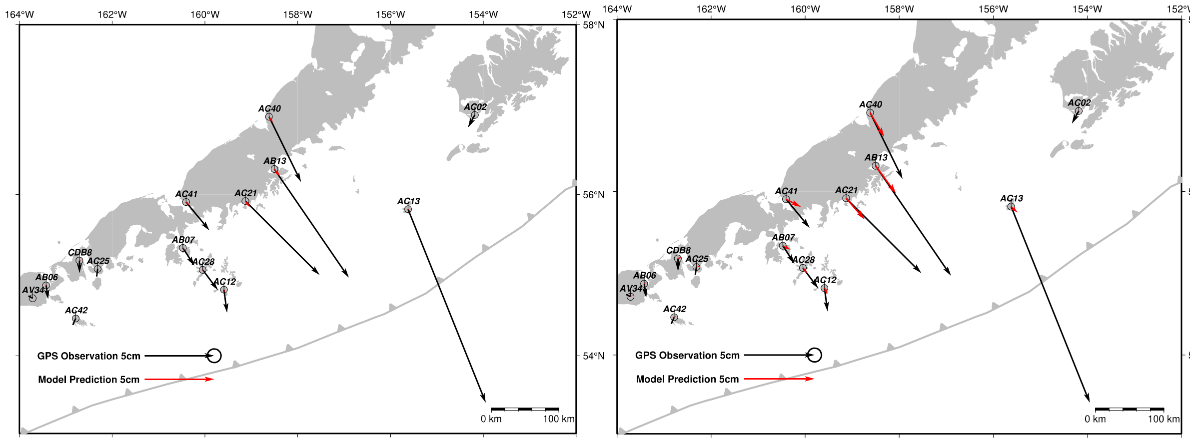

Figure 4. (a) Viscosity structure of minimum contribution of viscoelastic relaxation models. The blue region indicates the elastic lithosphere, the elastic slab and the code nose, the red region indicates the mantle wedge, the green region indicates the oceanic mantle and the rest of the continental mantle (b)Viscosity structure of maximum contribution of viscoelastic relaxation mode. The blue region indicates the elastic lithosphere and the elastic slab, the red region indicates the mantle wedge, the green region indicates the oceanic mantle and the rest of the continental mantle. (c), (d) The minimum and maximum predicted 3-month viscoelastic relaxation only horizontal displacements. The white barbed line shows the plate boundary between the Pacific plate and the North American plate.

We use the biviscous Burgers body to model the viscoelastic relaxation of the mantle wedge, as this model has been shown to improve fit to the postseismic data in many past studies. Following past studies (e.g., Tian et al., 2020; Huang et al., 2020), we assume that the viscosity of the Kelvin element of the Burger's body is 1/10 of the viscosity of the Maxwell element. We vary the Maxwell element viscosity in the range (1-5)*10^{19} Pa-s. Huang et al. (2019) found the value of the Maxwell viscosity of the mantle wedge to be 3*10^{19} Pa-s for the nearby 1964 Alaska earthquake. A higher value of viscosity of the mantle wedge will result in lower predicted displacements (Figure S1 a).

For the lithosphere thickness, the multichannel seismic (MCS) line ALEUT 3 (Kuehn, 2019) suggests an approximately 40km Moho depth for the overriding plate at the region of this earthquake. The mantle lithospheric thickness is not known, but needs to be added to the crustal thickness. We thus vary the lithospheric layer thickness between 40km and 50km given previous postseismic models for Alaska (e.g., Huang et al, 2020). A thicker lithospheric layer will result in lower predicted displacements (Figure S1 b).

Many studies have shown the significance of considering a cold nose in the viscoelastic relaxation modeling of subduction zone earthquakes (e.g., Sun et al., 2014; Lou et al., 2021). According to the thermal modeling of Syracuse et al. (2010), it is reasonable to assume the existence of an essentially elastic cold nose, although the extent of the cold nose is uncertain. Applying a cold nose will result in lower predicted displacements (Figure S1 c).

Nearly all of the predicted postseismic displacements result from relaxation of the mantle wedge material. We assumed a sub-oceanic mantle Maxwell viscosity of 10^{20} Pa-s, based on Huang et al. (2020) and Tian et al. (2020). However, if we made the sub-oceanic mantle to be elastic (infinite viscosity), the predicted signal does not change notably (Figure S1 d). Assuming a much lower viscosity for the sub-oceanic mantle mainly affects the vertical model prediction for sites near the updip end of the rupture, with little change to the horizontal predictions. Therefore, in this study we do not further consider variations in the sub-oceanic mantle viscosity.

4 Results

4.1 Comparison of Stress-driven Afterslip for Different Published Coseismic Rupture Models

We first compute afterslip-only models for each of the published coseismic slip models. We allow both up-dip and down-dip afterslip and also along-strike afterslip, but our observations are most sensitive to the downdip portion of the afterslip due to the distribution of GPS sites (Figure 1). Comparing the afterslip predictions (Figure 5), we find that the Liu et al. (2022), and Elliott et al. (2022), models both produce large azimuthal misfits at two peninsula sites AC21 and AB13, while the Ye et al. (2022) model, which has a more compact coseismic slip area, does not show this systematic misfit.

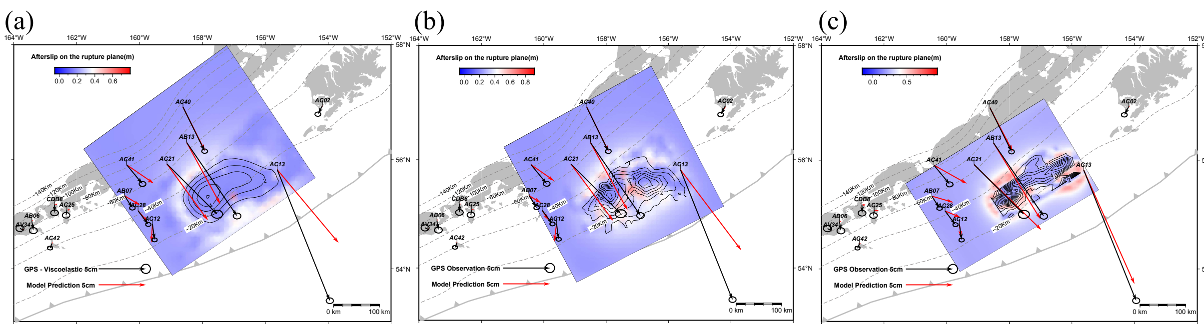

Figure 5. Best fit afterslip only models for published coseismic models (a) Elliott et al. (2022)model. (b) Liu et al.(2022) model (c) Ye et al. (2022) model. The error ellipse show 95% confidence. The region of the rupture areas is > 1m slip. Dashed light grey lines outlines the depth contours from the Slab2 model (Hayes et al., 2018). The white barbed line shows the plate boundary between the Pacific plate and the North American plate.

To assess the goodness of the post-seismic fit, we the utlilize near-field GPS continuous sites except for site AC13, while focusing on three peninsula sites (AB13, AC21, and AC40), for these three sites have large displacements and are most sensitive to the downdip distribution of afterslip. We are not evaluating the fit to site AC13 for two reasons. One is that it is not sensitive to the downdip afterslip (see the downdip-only afterslip model, Figure S2 a), and the other is that it is located at the edge of the rupture area, and its fast seaward motion might also include a contribution from other post-seismic mechanisms such as poroelastic rebound, which is beyond the scope of this paper. The sites close to the Shumagin islands (AC41, AB07, AC28, and AC12) have relatively small displacements and might be affected by the postseismic processes of the

July 21, 2020, Mw7.8 Simeonof earthquake, or by alternative assumptions about the distribution of velocity-strengthening material, so we will consider multiple misfit metrics to determine the best model.

The Ye et al. (2022) model differs from the other models in three ways. They assumed a deeper fault plane than the Slab2.0 geometry used by others, based on a seismic reflection study (Kuehn, 2019). Also, their slip model is more compact in the downdip direction, as a result of an assumption they made about the maximum possible depth of slip. Additionally, they added a patch of shallow slip near Chirikof Island in order to better explain the tsunami. This added slip patch, which was added to the slip model by those authors after their initial slip inversion, also makes their model predict the AC13 postseismic data better.

We estimated a new coseismic model by shifting the Elliott et al., (2022) model fault plane to be 6.5 km deeper, similar to the Ye et al. (2022) model geometry, but found that the coseismic slip (Figure S3i) and post-seismic displacement patterns (Figure S4) did not change much. However, when we tested a narrower fault model, by restricting the downdip extent of the model fault plane, we found that the fit to the postseismic data improved dramatically while the fit to the coseismic observations was nearly unchanged (Figure S3 b, Figure 6 b). These tests indicated that it is the narrower downdip width of the slip distribution that makes the Ye et al. (2022) model be a better predictor of the postseismic afterslip. A narrower fault model with a more abrupt decrease of the coseismic slip at the downdip end of the rupture plane results in afterslip being located farther offshore.

(a) (b)

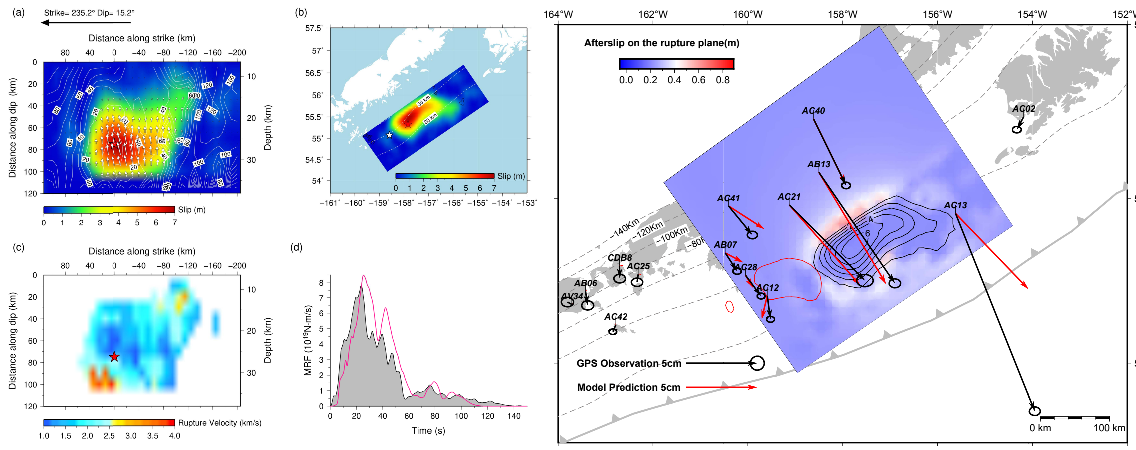

Figure 6. Preferred Coseismic model with 120km fault width(a) and its best fit afterslip-only model (b). The error ellipse show 95% confidence. The back and red contour indicate this earthquake and the 22 July 2020, Mw7.8 Simeonof earthquake, the region of the rupture areas is > 1m slip. Orange cycle scaled by magnitude indicates the 87 days aftershocks following this earthquake and the Simeonof earthquake, respectively. Dashed light grey lines outlines the depth contours from the Slab2 model (Hayes et al., 2018). The white barbed line shows the plate boundary between the Pacific plate and the North American plate.

Therefore, we investigated a series of alternative coseismic models with different model fault widths. In all cases, we fixed the up-dip limit of the fault plane to be the same as the Elliott et al. (2022) model, but varied the down-dip extent of the fault plane. We considered models with different downdip model fault plane widths of 100km, 110km, 120km, 130km, 140km, 150km, and 160km (the last is equal to that used by Elliott et al. (2022)). All models apply zero slip conditions beyond the edges of the model fault, and the bottom row of the subfaults also has a zero slip condition, so we report the width of the part of the fault plane that is actually allowed to slip. The models with narrower assumed fault widths force the slip distribution to be more compact and located farther offshore, and in general have a different character at the downdip limit of the coseismic rupture, with the models having narrower widths producing a more abrupt downdip limit of slip (Figure 7).

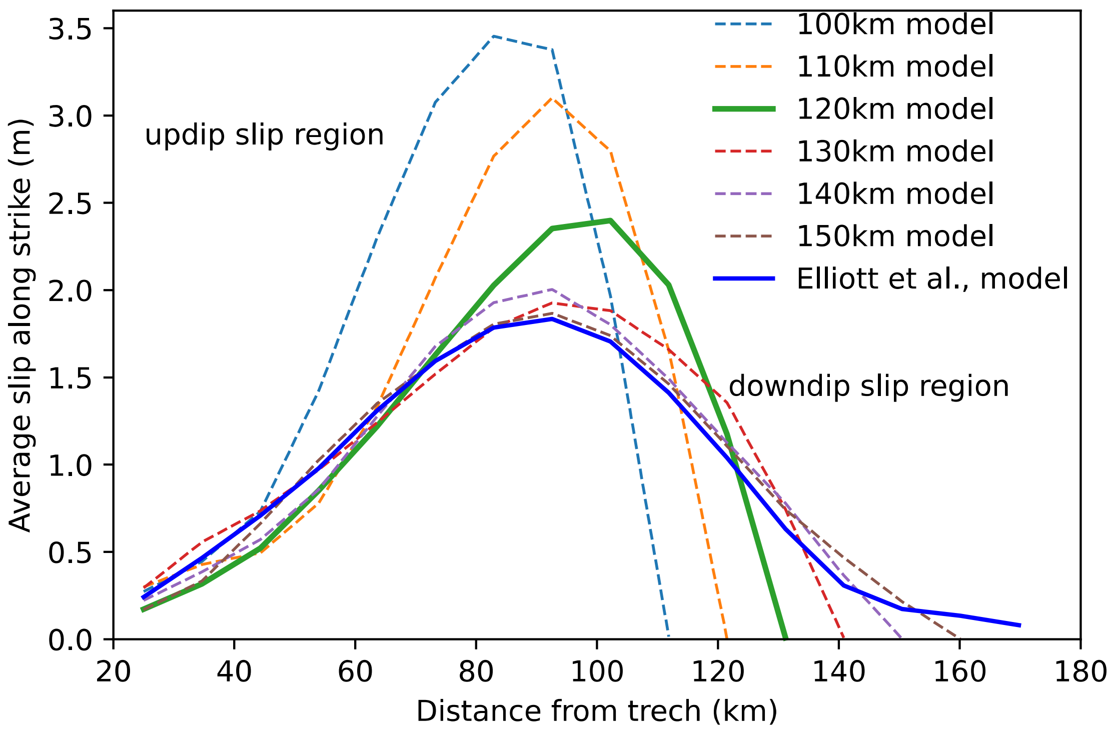

Figure 7. Average slip along strike of coseismic models with different fault width. Blue and green solid line outlines the comparison of the Elliott et al. (2022) model and our preferred coseismic model with 120km fault width.

We find that all of these models fit the coseismic data almost equally well (Figure S3 a-g), indicating that the coseismic data alone do not constrain these details of the coseismic slip distribution, due to limited model resolution arising from the sparsness and the spatial distribution of the data. As discussed later in sections 4.3 and 4.4, our preferred coseismic slip model (Figure 6) has a model fault 120 km wide in the downdip direction, similar to the Ye et al. (2022) model. The narrower fault models do not predict the coseismic vertical displacements as well as the wider models, but our tests indicate that making the model fault deeper could improve the fit to the vertical (Figure S3h). However, for simplicity we continue to use the Slab2.0-based fault geometry in the rest of this study.

4.2 3-Month Viscoelastic Relaxation Models with Different Assumed Viscosity Structures

In order to isolate afterslip, we simulate the potential viscoelastic relaxation contribution to the signal by testing different viscosity structures. We find that the viscoelastic relaxation predictions are not sensitive to the downdip distribution of the coseismic slip, because our models with different fault widths all give very similar viscoelastic model predictions (Figure S5). Based on this, we show here only the viscoelastic relaxation models for our preferred 120km-width coseismic model. The viscoelastic relaxation signal is smaller than the contribution of afterslip over this short time window, but it is not negligible for some models.

Using the method and model geometry described in section 3.2.2, we varied the value of Maxwell viscosity of the mantle wedge and the lithosphere thickness within the ranges given in section 3.2.2. We also varied whether or not there is a cold nose. For each viscoelastic model, we computed the displacements due to viscoelastic relaxation over the first three months after the earthquake. The geometry of our model can be found in Figure 4a, b.

Based on the three variations in the viscosity structure discussed above, we identified the viscosity structure that results in the maximum predicted displacements at sites on the Alaska Peninsula. That model has a Maxwell viscosity of the mantle wedge of 10^{19} Pa-s, a lithosphere thickness of 40km, and there is no cold nose. We also identified the viscosity structure that results in the minimum predicted displacements. That model has a Maxwell viscosity of the mantle wedge of $5*10^{19}$ Pa-s, a lithosphere thickness of 50km, and a cold nose that extends to 80km depth. In the latter case, the prediction of viscoelastic relaxation is very small and can be ignored, so the post-seismic signals could be regarded as being due only to afterslip in that case. Figure 4 shows the geometry and viscosity structure of these two upper and lower bound viscoelastic relaxation models and their corresponding surface displacement predictions.

4.3 3-Month Afterslip-Only Models with Different Fault Widths Assumed

Because even the viscoelastic models with maximum displacement have relatively small amplitudes compared to the data, it is useful to start by considering afterslip-only models. The models with the minimum potential viscoelastic relaxation contribution subtracted are equivalent to afterslip-only models, because the viscoelastic relaxation contribution for that viscoelastic model is negligible.

The first important question to address for the afterslip-only models is, where is the afterslip allowed to occur? The edge of the west portion of the Chignik earthquake rupture plane is adjacent to the coseismic rupture area of the Mw7.8 Simeonof earthquake. If that part of the fault has velocity-weakening friction, there should be no afterslip allowed within the coseismic rupture region of the Simeonof earthquake. However, we find that allowing afterslip there or not does not significantly affect our predictions for the sites outside of the Shumagin Islands (Figure S6). Thus, we first considered three scenarios of afterslip forward models: allowing the afterslip to occur up-dip only, down-dip only, and fully surrounding the coseismic rupture zone, using the coseismic model of Elliott et al. (2022), and we focus on the predicted displacements on the Alaska Peninsula. None of these models predict the displacement of site AC13 well, although the Ye et al. (2022) model with its relatively isolated large patch of shallow slip very close to AC13 does fairly well.

Figure S2a shows that the downdip-only afterslip model can easily explain the displacements along the Alaska Peninsula. Downdip afterslip contributes almost nothing to the signal at AC13, which must be explained by some combination of updip afterslip and perhaps poroelastic relaxation. Figure S2b shows that the updip-only afterslip model predicts displacements at Peninsula sites AB13 and AC40 that are much smaller than the observations for any V_0 value, because the total stress change is not able to generate enough afterslip to match the observed displacements there. Thus, for simplicity our preferred model is that afterslip is allowed to fully surround the coseismic rupture zone. Changing the updip frictional parameters would have only a minimal impact on our model predictions, except at AC13.

We then use the coseismic rupture models with different assumed fault widths that we obtained from section 4.1 as input for a series of afterslip-only models. We find that using the coseismic model with a fault width of 120km significantly reduces the azimuthal misfit of the two peninsula sites AB13 and AC40, with the best fit model having a minimum reduced χ^2 of 16.27 when considering all data (Figure 8). The same model has the minimum misfit whether we consider only the Peninsula sites or include the Shumagin sites as well. A slightly narrower model (110 km width) minimizes the angular misfit of the displacements for AB13 and AC21. The frictional parameters we find for this preferred model are $a\sigma$ =0.60MPa, V_0 = 0.82m/yr.

Figure 9 shows the best fit afterslip only models for coseismic models with different fault widths. The postseismic fit is hugely improved by reducing the fault widths, so that afterslip occurs further offshore (Figure 10). This indicates that the postseismic observations give important new constraints to the coseismic slip model.

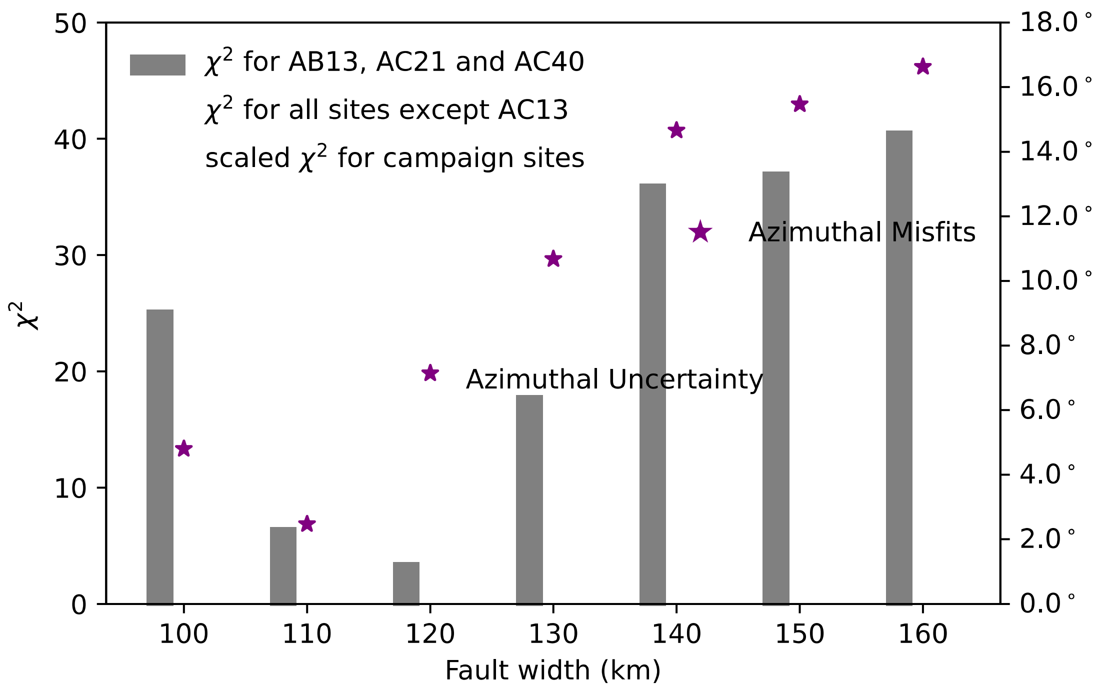

Figure 8. Visualization of reduced χ^2 for various coseismic fault models. The bars represent the χ^2 values, while the azimuthal misfits are represented by purple stars. The azimuthal uncertainty represents the allowable error in the azimuth when the model prediction arrow falls within the GPS data error ellipse.

(a)

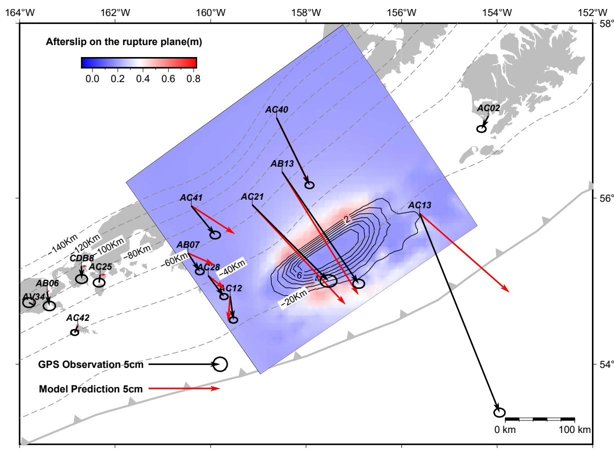

(b)

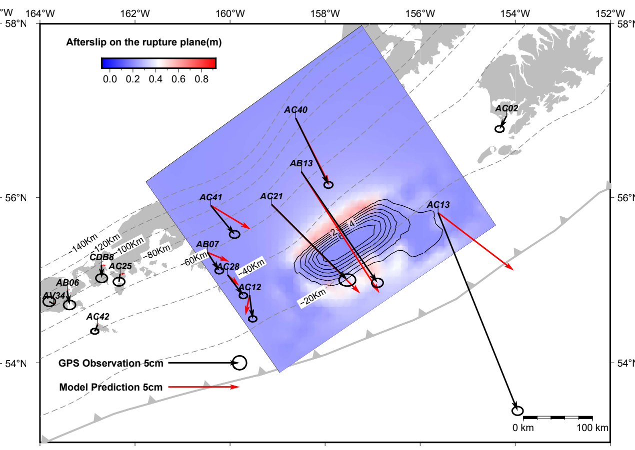

(c)

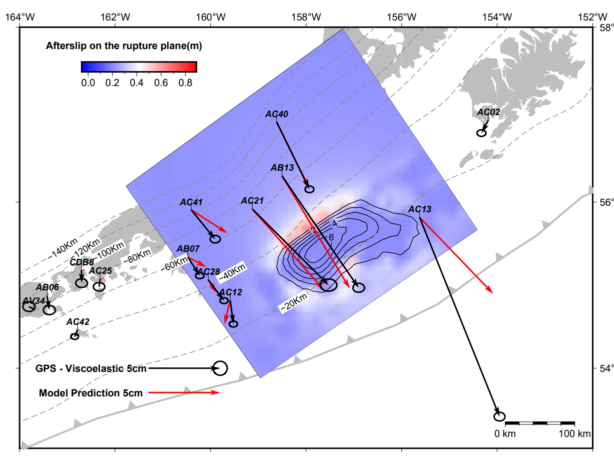

(d)

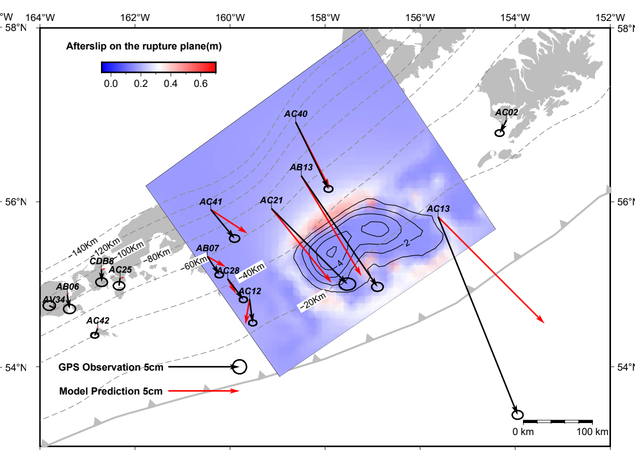

(e)

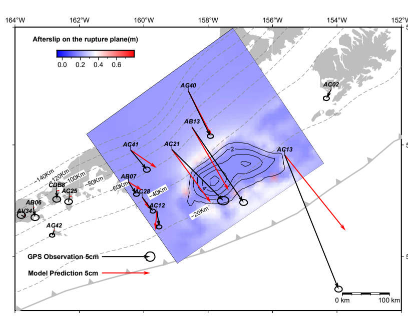

(f)

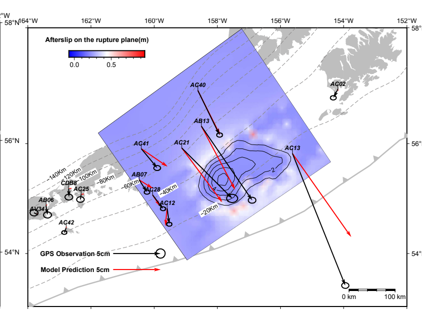

(g)

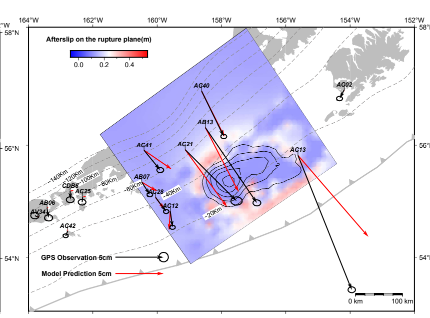

Figure 9. Best fit afterslip-only models for coseismic models with different fault width. (a) 100km coseismic fault width. (b) 110km coseismic fault width. (c) 120km coseismic fault width. (d) 130km coseismic fault width. (e) 140km coseismic fault width. (f) 150km coseismic fault width. (g) 160km coseismic fault width. The region of the rupture areas is > 1m slip. Dashed light grey lines outlines the depth contours from the Slab2 model (Hayes et al., 2018). The white barbed line shows the plate boundary between the Pacific plate and the North American plate.

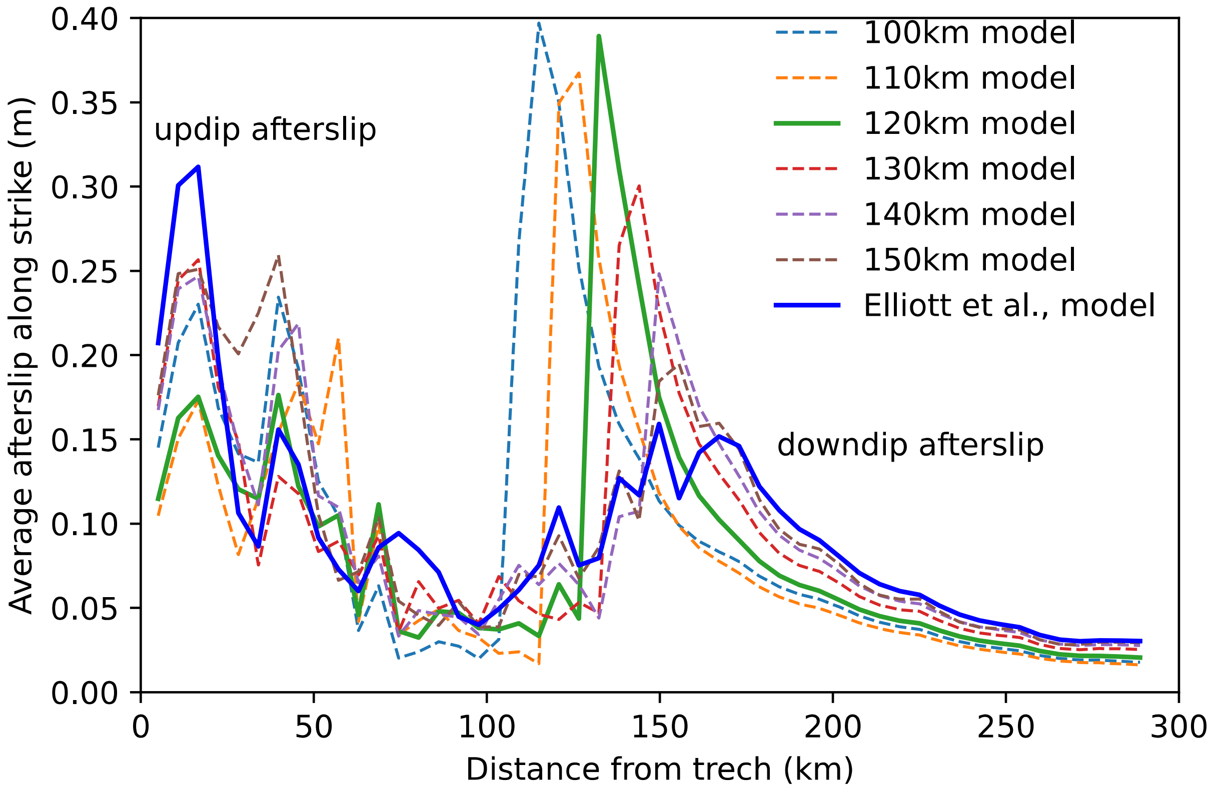

Figure 10. Average afterslip along strike of coseismic models with different fault width. Blue and green solid line outlines the comparison of the Elliott et al., 2022 model and our preferred coseismic model with 120km fault width.

4.4 3-Month Afterslip Models with Maximum Viscoelastic Relaxation Contribution Assumed.

We evaluated a range of viscoelastic relaxation models, and consider end members with the minimum and maximum displacements caused by that mechanism as described in section 4.2; the minimum contribution being negligible and thus equivalent to the afterslip-only models already described. For the model with the maximum contribution from viscoelastic relaxation, we subtracted the viscoelastic model prediction from the data and treated the residual as the afterslip contribution. We then ran the same tests as described in section 4.3, and find that even with the maximum viscoelastic relaxation contribution considered, our afterslip models also favors a narrower fault width with 120km width. In this case, the overall minimum χ^2 is 9.02, lower than for afterslip-only. The best fit V_0 is smaller than the models without a viscoelastic contribution, with V_0 = 0.45m/yr. Figure 11 shows the best fit afterslip models with maximum viscoelastic relaxation prediction for coseismic models with fault widths of 100km, 120km, 130km and 160km.

(a) (b) (c)

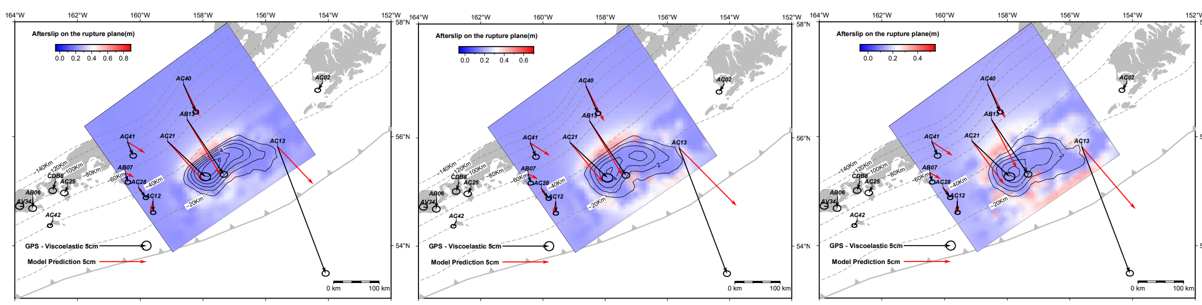

Figure 11. Best fit afterslip models with maximum viscoelastic relaxation contribution subtracted for coseismic models with different fault width. (a) 120km coseismic fault width. (b) 130km coseismic fault width (c) 160km coseismic fault width. The error ellipse show 95% confidence. The region of the rupture areas is > 1m slip. Dashed light grey lines outlines the depth contours from the Slab2 model (Hayes et al., 2018). The white barbed line shows the plate boundary between the Pacific plate and the North American plate.

4.5 3-Week Postseismic + Coseismic Fit at the GPS Campaign Sites.

We also consider a second data set to further validate our conclusion that the coseismic slip distribution must be compact in the downdip direction, so that afterslip remains sufficiently far offshore. It is possible that the stress-driven afterslip could occur within the coseismic rupture area due to complex frictional properties, or a complex coseismic slip distribution (Johnson et al., 2012, Avouac 2015). Thus, we also use displacements from campaign GPS sites measured three weeks after the mainshock, which include coseismic slip plus three weeks of postseismic deformation. We consider the same range of coseismic slip models as in the previous sections.

For each coseismic slip model, we compute stress-driven afterslip and use the measured 3-week displacements from the continuous GPS sites to search for the best afterslip frictional parameter V_0, using the same method as for the 3-month case. Then we compare the coseismic displacements plus the predicted 3-week postseismic displacements to the observed coseismic + 3-week postseismic displacements at the GPS campaign sites. Viscoelastic relaxation is negligible over the first three weeks, based on the models already discussed above. Again, we find that a narrower fault of 110km~140km is preferred (light orange bars in Figure 8). This model also reduces the angular misfit at two island campaign sites with large displacements (YUK and SEMI) (Figure 12). This provides further support for our conclusion that the postseismic observations require a relatively compact rupture in the downdip direction.

(a) (b) (c)

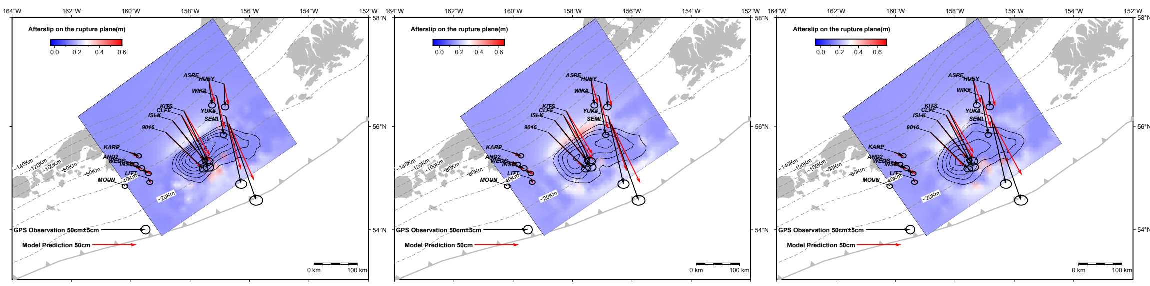

Figure 12. GPS observations at campaign sites and 3-week afterslip model predictions + coseismic model predictions with different fault width assumed. (a) 120km coseismic fault width. (b) 130km coseismic fault width (c) 150km coseismic fault width. The error ellipse show 95% confidence. The region of the rupture areas is > 1m slip. Dashed light grey lines outlines the depth contours from the Slab2 model (Hayes et al., 2018). The white barbed line shows the plate boundary between the Pacific plate and the North American plate.

5. Discussion

5.1 The downdip limit of the coseismic rupture

All of the models that predict the postseismic displacements well have a slip distribution that is located well offshore. They also have a relatively abrupt downdip termination of slip, and a clean separation between the zones of coseismic slip and afterslip (Figures 6, 9). Because the basic characteristics of the slip models are not very sensitive to assumed fault depth, and there is some uncertainty in the geometry and depth of the plate interface, the horizontal location of the downdip end of the rupture is determined more precisely than the depth.

Figure 1 shows comparisons between the co-seismic slip region of the Elliott et al. (2022) model and our preferred 120km fault width model, along with the aftershock distribution. The aftershock region matches more closely to the slip area with our preferred narrower fault than with the original Elliott et al. (2022) model. Based on our preferred coseismic rupture model, the downdip afterslip did not trigger a significant number of downdip aftershocks. This suggests that the coseismic rupture extended in depth to the deepest extent of the velocity-weakening friction, or beyond it given stress shadowing effects (e.g., Lindsey et al., 2021).

There are several clusters of aftershocks updip of the coseismic rupture, which we interpret to be triggered by the updip afterslip. The existence of these aftershock clusters suggests that some of the fault plane updip of the coseismic rupture likely has velocity-weakening frictional behavior.

5.2 Vertical Postseismic Signals over the first 3 months

Although we didn't use the vertical signal in the previous discussion due to the larger uncertainties and the relatively small signal, the vertical signal further supports our conclusion of a narrower coseismic rupture, and provides some preliminary information about the viscosity structure. We do not fully explore the tradeoffs between parameters in the viscoelastic model here, because the timespan of the data is very short. However, we can use the vertical data to find a reasonable combination of lithospheric thickness, mantle wedge viscosity, and cold nose structure that can serve as a reference model for future modeling.

Figure 13 a, b shows the observed post-seismic vertical displacement, the vertical displacement due to an afterslip-only model and the vertical displacement due to a viscoelastic relaxation-only model. The predicted vertical displacement due to the afterslip-only model at all Alaska

Peninsula sites is subsidence. The viscoelastic relaxation-only model predicts uplift at those same sites. In both cases, the model predictions are substantially larger than the observed displacements at the Peninsula sites AB13 and AC21, so matching the observations requires a contribution from both mechanisms. The two Peninsula sites AB13 and AC21 are close to each other, but we observe subsidence at the site AC21and uplift at the site AB13. The signals are small amplitude, indicating the subsidence displacement predicted by the afterslip and the uplift displacement predicted by the viscoelastic relaxation must share a similar absolute value at those two sites, but of opposite sign. This requires a non-negligible viscoelastic relaxation contribution to the observed signal. Therefore, we explore the range of our test models to find a reasonable model that might explain the vertical data.

(a) (b)

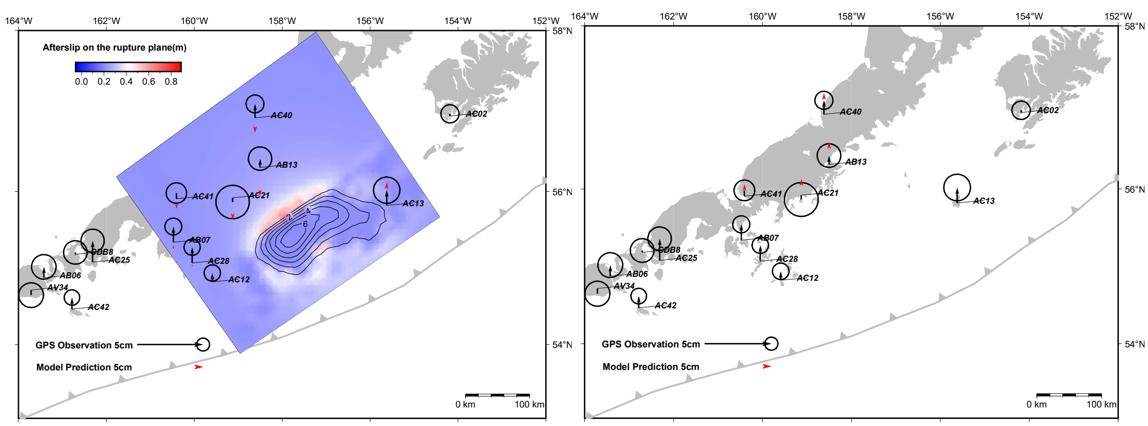

Figure 13. (a) 3- month vertical prediction of an afterslip-only model. The coseismic fault width is 120km. (b) 3-month vertical prediction of a viscoelastic relaxation only model. The viscosity structure is 50km LAB, having a cold nose to the wedge and the wedge Maxwell viscosity is $5*10^{18}$ Pa-s. The error ellipse show 95% confidence. The region of the rupture areas is > 1m slip. Dashed light grey lines outlines the depth contours from the Slab2 model (Hayes et al., 2018). The white barbed line shows the plate boundary between the Pacific plate and the North American plate.

Figure S7 shows the predicted vertical signal of viscoelastic-only models based on different assumed viscosity structures, and Figure S8 shows the predicted vertical signal of afterslip-only models based on different fault widths. The observed displacement at site AC40 is about 1 cm uplift, and all of our afterslip models with different fault widths assumed predict about 1cm subsidence; this requires a ~2cm uplift contribution from viscoelastic relaxation at site AC40. Our maximum viscoelastic relaxation contribution model used above (40km LAB + 10^{19} Pa-s wedge viscosity and no cold nose) only predicts ~0.5cm uplift at site AC40, but a different combination of model parameters might produce a larger uplift.

Figure S7 and Figure S1 show that by increasing the LAB depth and adding a cold nose to the wedge, the model predicts more uplift and a smaller horizontal displacement at site AC40. Thus, a cold nose to the wedge and a deeper LAB than used in our models is needed in order to get a predicted ~2cm uplift from viscoelastic relaxation at site AC40, although this also would require a lower mantle wedge viscosity. Together with afterslip, such a model can predict the observed vertical displacement with a Maxwell viscosity of the mantle wedge of $5*10^{18}$ Pa-s. Thus, we consider a reasonable model to have that viscosity with a 50km lithosphere thickness, a cold nose to the wedge. Because of a tradeoff between the lithosphere thickness (and cold nose geometry) and asthenospheric viscosity, a model with a lower viscosity can give about the same horizontal displacements as the models discussed earlier, although the vertical displacements and also far-field displacements will differ.

We computed the horizontal displacement of the viscoelastic relaxation based on this viscosity structure and subtracted that from the GPS observations. We use the residuals to search for the best-fit afterslip model based on the 120km coseismic fault. Finally, we add together the vertical prediction of viscoelastic-only model and afterslip-only model and compare that to the observations. Figure 14 shows the horizontal viscoelastic relaxation only prediction, the afterslip horizontal fit and the total vertical fit. The model is a reasonable fit to both the vertical and horizontal observations, but needs to be tested with a longer time span of data and data from sites farther from the rupture, and the parameter tradeoffs explored more thoroughly. In particular, there are strong tradeoffs between the geometry of the cold nose, lithospheric thickness, and wedge viscosity. These will be easier to explore at later times when the afterslip contribution is smaller.

(a) (b) (c)

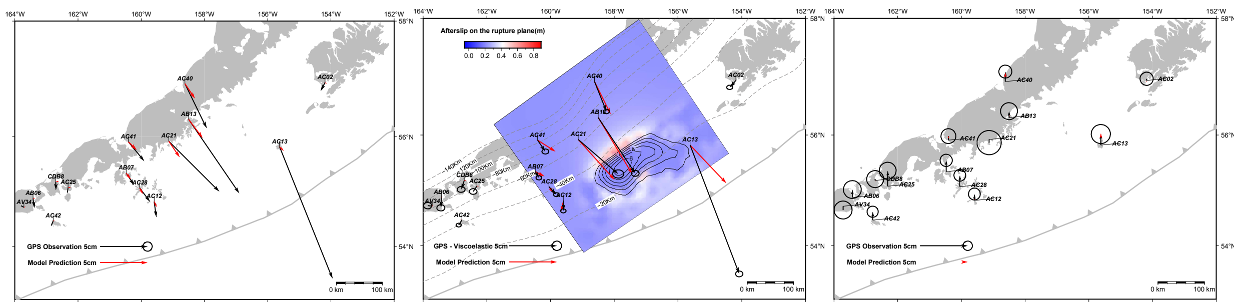

Figure 14. (a) horizontal prediction of 3-month viscoelastic relaxation-only model for the 120km coseismic fault based on the viscosity structure of 50km LAB, having a cold nose to the wedge and the $5*10^{18}$ Pa-s wedge viscosity. (b) Best fit afterslip model based on the signal residual (GPS observation – viscoelastic relaxation contribution). (c) total vertical fit (model prediction = afterslip prediction + viscoelastic relaxation prediction). The error ellipse show 95% confidence. The region of the rupture areas is > 1m slip. Dashed light grey lines outlines the depth contours from the Slab2 model (Hayes et al., 2018). The white barbed line shows the plate boundary between the Pacific plate and the North American plate.

5.3 Comparison of Coseismic Slip to the July 22, 2020, Mw7.8 Simeonof Earthquake

Figure 6 shows the coseismic slip contours of our preferred 120km coseismic rupture model for the 2021 Chignik earthquake, and the 2020 Simeonof earthquake from Xiao et al. (2021). Aftershocks that followed both earthquakes are shown. The July 21, 2020 Mw7.8 Simeonof Shumagin earthquake is thought to have ruptured to greater depth alongat the subduction zone interface (e.g., Shillington et al. 2022), and also have has a deeper aftershock region, than the Chignik earthquake. That greater depth only applies to the western half of the 2020 rupture. This difference in the down-dip extent of the coseismic rupture plane, as well as the down-dip extent of aftershocks might indicate a significant frictional property difference (e.g., Shillington et al., 2015; Li et al., 2018; Becel et al., 2017) between the Semidi and the Shumagin segments, as suggested by the interseismic coupling studies (e.g., Drooff and Freymueller, 2021; Xiao et al., 2021)

5.4 Constraints on the Updip Coseismic Slip Distribution and Postseismic Mechanisms

The updip portion of the published coseismic slip models varies considerably (Figures 2, 7), and it remains unclear which model better resolves the up-dip portion of the coseismic slip. The Ye et al. (2022) and Liu et al. (2023) models used tsunami data to iteratively adjust the coseismic model. These models differ from the Elliott et al. (2022), Liu et al. (2022) and Mulia et al. (2022) model in having a distinct slip patch that has very large slip magnitude (~ 10m) and a rake of 45 degree under Chirikof island. Aside from that shallow patch, the Ye et al. (2022) and Liu et al. (2023) models overall restrict slip to greater depths than do the Elliott et al. (2022) model, or the models shown here. However, the solutions that fit the tsunami data are not unique. Liu et al., (2023) Figure S7 shows that the Elliott et al., (2022) model, which has about ~1m slip extending slightly beyond the continental shelf break, also fits the tsunami data well. Brooks et al. (2023) modeled the coseismic (and 2.5 month postseismic) displacement from a GNSS-Acoustic site seaward of the Chignik rupture and have also argued for greater slip extending to shallower depths than some of the models proposed, although the slip could be in the form of rapid shallow afterslip.

It is more difficult to constrain the up-dip post-seismic slip compared to the downdip portion. The main limitation is that we only have one GPS continuous site, AC13, at the updip end of the coseismic rupture area. Stress-driven afterslip models do not predict the very large postseismic displacement at AC13, unless they include a large coseismic slip patch very close to AC13 (like the Ye et al., (2022) and Liu et al., (2023) models). However, considering the magnitude of this earthquake and the location of site AC13, the effects of poroelastic relaxation, depth variations in the frictional parameters (e.g., Tian et al. (2023)), and the potential existence of a weak sub-slab oceanic mantle layer could also affect the model prediction. Thus, there could be considerable non-uniqueness in the model. Due to the limited number of GPS sites located at the updip end of the coseismic rupture, it is difficult to fully separate the postseismic mechanisms, making it also difficult to assess the exact contribution of shallower afterslip and the shallower portion of coseismic slip of this event. A significant expansion of seafloor geodesy will be required to answer those remaining questions.

6. Conclusions

We generated a suite of coseismic slip models for the 29 July 2021, Mw 8.2 Chignik earthquake by inverting seismic and geodetic data, and varying the assumed downdip end of the coseismic plane. Models with a narrower allowed downdip width have slip located farther offshore, and have a more abrupt downdip termination of slip, while models that allow a wider rupture have slip that tapers to zero more gradually with depth.

For each model, we computed stress driven afterslip models and viscoelastic relaxation models, and compared the postseismic model predictions to observed postseismic displacements over the first 3 months after the earthquake. As long as the frictional properties are uniform, the spatial pattern and relative magnitudes of postseismic afterslip displacements are determined entirely by the coseismic slip distribution, while the rate of early postseismic slip and its time decay depend on the values of the frictional parameters chosen. The predicted afterslip displacement pattern is significantly different for the different coseismic models, but the predicted viscoelastic relaxation deformation is not.

We find that the coseismic data alone cannot resolve the details of slip at the downdip end of the rupture, but the postseismic displacements provide important new information. By limiting the model fault plane width to 120km downdip, the observed post-seismic signal is much better explained with stress-driven afterslip for all reasonable viscoelastic relaxation contributions considered. A model with a narrower downdip extent of slip, and thus a more abrupt downdip termination of slip, produces afterslip located farther offshore, and this is necessary to match the orientations of the observed postseismic displacements. This finding holds for all reasonable contributions from viscoelastic relaxation, including models where the viscoelastic signal is negligible. However, overall data fit is improved when a combination of stress-driven afterslip and viscoelastic relaxation is included in the model, and this combination makes it possible to explain the vertical displacements as well as the horizontal.

The preferred coseismic rupture plane with a 120km fault width also has a much better model-data fit for the 3-week coseismic + post-seismic deformation at GPS campaign sites (Figure 8), in which time period the coseismic signal should be the dominant, which further confirms that the spatial pattern of stress-driven afterslip brings new information of the coseismic rupture of the 29 July 2021, Mw 8.2 Chignik earthquake.

Our results indicate an abrupt instead of gradual downdip termination of coseismic slip. The lack of deep aftershocks further supports this conclusion and suggests that there was limited interseismic slip deficit deeper than the coseismic rupture, even accounting for stress-shadowing effects, in line with the Xiao et al. (2021) coupling model for this region.

Acknowledgments

This material is based on services provided by the GAGE Facility, operated by EarthScope Consortium, with support from the National Science Foundation, the National Aeronautics and Space Administration, and the U.S. Geological Survey under NSF Cooperative Agreement EAR-1724794. The facilities of EarthScope (IRIS) Data Services, and specifically the Data Management Center, were used for access to waveforms, related metadata, and/or derived products used in this study. EarthScope Data Services are funded through the Seismological Facilities for the Advancement of Geoscience (SAGE) Award of the National Science Foundation under Cooperative Support Agreement EAR-1851048. This research was supported by NSF awards EAR-2052558, EAR-2147422, and EAR-2152253 to Michigan State University, and the MSU Solid Earth Endowment, and EAR-2052569, NASA-ESI 80NSSC20K0761 to University of Alaska Fairbanks.

Open Research

Global seismic waveforms used for coseismic joint inversion were downloaded from the EarthScope Consortium (IRIS) Wilber 3 System (http://ds.iris.edu/wilber3/find_event) and included data from the following seismic networks: (1) the G (GEOSCOPE; IPGP/EOST); (2) the IC (NCDSN; ASL/USGS, 1992); (3) the IM; (4) the IU (GSN; IRIS/USGS, 1988); (5) the MN (MetNet; INGV, 1990); (6) the CI (SCSN; Caltech/USGS, 1926); (7) the CN (CNSN; NRCAN, 1975); (8) the II (GSN; IRIS/IDA, 1986); (9) the GE (GEOFON; GFZ-Potsdam, 1991); and (10) the HK. References. Raw GNSS data used in this study are available at the GAGE Facility archive, operated by EarthScope Consortium (UNAVCO) (http://www.unavco.org) or through the National Geodetic Survey (https://geodesy.noaa.gov/CORS/). The aftershock catalog was downloaded from USGS (https://earthquake.usgs.gov/earthquakes/map/).

References

Abers, G. A., van Keken, P. E., & Hacker, B. R. (2017). The cold and relatively dry nature of mantle forearcs in subduction zones. Nature Geosci- ence, 10(5), 333–337. https://doi.org/10.1038/ngeo2922

Avouac, J.P., 2015. From geodetic imaging of seismic and aseismic fault slip to dy- namic modeling of the seismic cycle. Annu. Rev. Earth Planet. Sci. 43, 233–271. https://doi.org/10.1146/annurev-earth-060614-105302.

Barbot, S., Fialko, Y., & Bock, Y. (2009). Postseismic deformation due to the Mw 6.0 2004 Parkfield earthquake: Stress-driven creep on a fault with spatially variable rate-and-state friction parameters. Journal of Geophysical Research, 114, B07405. https://doi.org/10.1029/2008JB005748

Barbot, S., Moore, J. D. P., & Lambert, V. (2017). Displacement and stress associated with distributed anelastic deformation in a half - space. Bulletin of the Seismological Society of America, 107(2), 821‐855. https://doi.org/10.1785/0120160237

Bécel, A., Shillington, D. J., Delescluse, M., Nedimović, M. R., Abers, G. A., Saffer, D. M., Webb, S. C., Keranen, K. M., Roche, P. H., Li, J., & Kuehn, H. (2017). Tsunamigenic structures in a creeping section of the Alaska subduction zone. Nature Geoscience, 10(8), 609– 613. https://doi.org/10.1038/ngeo2990

Benjamin A. Brooks et al. ,Rapid shallow megathrust afterslip from the 2021 M8.2 Chignik, Alaska earthquake revealed by seafloor geodesy. Sci.Adv.9,eadf9299(2023).DOI:10.1126/sciadv.adf9299

Bertiger, W., Bar-Sever, Y., Dorsey, A., Haines, B., Harvey, N., Hemberger, D., et al., 2020. GipsyX/RTGx, a new tool set for space geodetic operations and research. Adv. Space Res. 66 (3), 469–489. https://doi.org/10.1016/j.asr.2020.04.015.

Bürgmann, R., Pollard, D. D., & Martel, S. J. (1994). Slip distributions on faults: Effects of stress gradients, inelastic deformation, heterogeneous host-rock stiffness, and fault interaction. Journal of Structural Geology, 16(12), 1675–1690. https://doi.org/10.1016/0191-8141(94)90134-1

Cross, R. S., & Freymueller, J. T. (2008). Evidence for and implications of a Bering plate based on geodetic measurements from the Aleutians and Western Alaska. Journal of Geophysical Research, 113, B07405. https://doi.org/10.1029/2007JB005136

Davies, J., Sykes, L., House, L., & Jacob, K. (1981). Shumagin seismic gap, Alaska Peninsula: History of great earthquakes, tectonic setting,and evidence for high seismic potential. Journal of Geophysical Research, 86(B5), 3821–3855. https://doi.org/10.1029/JB086iB05p03821

DeMets, C., Gordon, R. G., & Argus, D. F. (2010). Geologically current plate motions. Geophysical Journal International, 181, 1–80. https://doi.org/10.1111/j.1365-246x.2009.04491.x

Droof, C., & Freymueller, J. T. (2021). New constraints on slip deficit on the Aleutian megathrust and inflation at Mt. Veniamino, Alaska from repeat GPS measurements. Geophysical Research Letters, 48, e2020GL091787. https://doi.org/10.1029/2020GL091787

Elliott, J., & Freymueller, J. T. (2020). A block model of present-day kinematics of Alaska and Western Canada. Journal of Geophysical Research: Solid Earth, 125, e2019JB018378. https://doi.org/10.1029/2019JB018378

Elliott, J. L., Grapenthin, R., Parameswaran, R. M., Xiao, Z., Freymueller, J. T., & Fusso, L. (2022). Cascading rupture of a megathrust. Science Advances, 8(18), eabm4131. https://doi.org/10.1126/sciadv.abm4131

Fournier, T.J., Freymueller, J.T., 2007. Transition from locked to creeping subduction in the Shumagin region, Alaska. Geophys. Res. Lett. 34 (6) https://doi.org/10.1029/2006GL029073.L06303.

Freymueller, J. T., Suleimani, E. N., & Nicolsky, D. J. (2021). Constraints on the slip distribution of the 1938 MW 8.3 Alaska Peninsula earthquake from tsunami modeling. Geophysical Research Letters, 48, e2021GL092812. https://doi.org/10.1029/2021GL092812

Freymueller, J. T., Woodard, H., Cohen, S. C., Cross, R., Elliott, J., Larsen, C. F., et al. (2008). Active deformation processes in Alaska, based on 15 years of GPS measurements. In J. T.Freymueller, P. J.Haeussler, R. L.Wesson, & G.Ekström (Eds.), Active tectonics and seismic potential of Alaska (Vol. 179, pp. 1–42). https://doi.org/10.1029/179GM02

Fukuda, J., & Johnson, K. M. (2021). Bayesian inversion for a stress-driven model of afterslip and viscoelastic relaxation: Method and application to postseismic deformation following the 2011 MW 9.0 Tohoku-Oki earthquake. Journal of Geophysical Research: Solid Earth, 126, e2020JB021620.https://doi.org/10.1029/2020JB021620

Harvey, D. Hemberger, M. Heflin, W. Lu, M. Miller, A. W. Moore, et al. (2020). GipsyX/RTGx, a new tool set for space geodetic operations and research, Advances in Space Research 66, no. 3, 469–489, doi: 10.1016/j.asr.2020.04.015.

Hayes, G. P., Moore, G. L., Portner, D. E., Hearne, M., Flamme, H., Furtney, M., & Smoczyk, G. M. (2018). Slab2, a comprehensive subduction zone geometry model. Science, 362(6410), 58–61. https://doi.org/10.1126/science.aat4723

Hu, Y., Bürgmann, R., Freymueller, J. T., Banerjee, P., & Wang, K. (2014). Contributions of poroelastic rebound and a weak volcanic arc to the postseismic deformation of the 2011 Tohoku earthquake. Earth, Planets and Space, 66(1), 106. https://doi.org/10.1186/1880-5981-66-106

Hu, Y., & Freymueller, J. T. (2019). Geodetic observations of time - variable Glacial Isostatic Adjustment in southeast Alaska and its implications for Earth rheology. Journal of Geophysical Research: Solid Earth, 124(9), 9870-9889. https://doi.org/10.1029/2018JB017028

Huang, K., Hu, Y., & Freymueller, J. T. (2020). Decadal viscoelastic postseismic deformation of the 1964 Mw9.2 Alaska earthquake. Journal of Geophysical Research: Solid Earth, 125, e2020JB019649. https://doi.org/10.1029/2020JB019649

Ji, C., D. J. Wald, and D. V. Helmberger (2002), Source description of the 1999 Hector Mine, California, earthquake, Part I: Wavelet domain inversion theory and resolution analysis, Bull. Seismol. Soc. Am., 92(4), 1192– 1207.

Johnson, K. M., Fukuda, J., & Segall, P. (2012). Challenging the rate-state asperity model: Afterslip following the 2011 M9 Tohoku-oki, Japan, earthquake. Geophysical Research Letters, 39, L20302. https://doi.org/10.1029/2012GL052901

Johnson, K. M., Bürgmann, R., & Freymueller, J. T. (2009). Coupled afterslip and viscoelastic flow following the 2002 Denali Fault, Alaska earthquake. Geophysical Journal International, 176(3), 670–682. https://doi.org/10.1111/j.1365246X.2008.04029.x

Li, J., Shillington, D. J., Bécel, A., Nedimović, M. R., Webb, S. C., Saffer, D. M., et al. (2015). Downdip variations in seismic reflection charac- ter: Implications for fault structure and seismogenic behavior in the Alaska subduction zone. Journal of Geophysical Research: Solid Earth, 120(11), 7883–7904. https://doi.org/10.1002/2015JB012338

Li, J., Shillington, D. J., Saffer, D. M., Bécel, A., Nedimović, M. R., Kuehn, H., et al. (2018). Connections between subducted sediment, pore-fluid pressure, and earthquake behavior along the Alaska megathrust. Geology, 46(4), 299–302. https://doi.org/10.1130/G39557.1

Lindsey, E. O., R. Mallick, J. A. Hubbard, K. E. Bradley, R. Almeida, J. D. P. Moore, R. Burgmann, and E. M. Hill, Slip rate deficit and earthquake potential on shallow megathrusts, Nature Geoscience, doi:10.1038/s41561-021-00736-x, 2021.

Li, S., Freymueller, J.T., 2018. Spatial variation of slip behavior beneath the Alaska Peninsula along Alaska-Aleutian subduction zone. Geophys. Res. Lett. 45 (8), 3453–3460. https://doi.org/10.1002/2017GL076761.

Liu, C., Lay, T., & Xiong, X. (2022). The 29 July 2021 MW 8.2 Chignik, Alaska Peninsula earthquake rupture inferred from seismic and geodetic observations: Re-Rupture of the Western 2/3 of the 1938 rupture zone. Geophysical Research Letters, 49, e2021GL096004. https://doi.org/10.1029/2021GL096004

Liu, C., Bai, Y., Lay, T., Feng, Y., Xiong, X. (2023) Megathrust complexity and the up-dip extent of slip during the 2021 Chignik, Alaska Peninsula earthquake, Tectonophysics, https://doi.org/10.1016/j.tecto.2023.229808.

Luo, H., & Wang, K. (2021). Postseismic geodetic signature of cold forearc mantle in subduction zones. Nature Geoscience, 14, 104–109. https://doi.org/10.1038/s41561-020-00679-9

Mulia, I. E., Gusman, A., Heidarzadeh, M., & Satake, K. (2022). Sensitivity of tsunami data to the up-dip extent of the July 2021 Mw 8.2 Alaska earthquake. Seismological Research Letters, 93(4), 1992–2003. https://doi.org/10.1785/0220210359

Muto, J., Moore, J. D. P., Barbot, S., Iinuma, T., Ohta, Y., & Iwamori, H. (2019). Coupled afterslip and transient mantle flow after the 2011 Tohoku earthquake. Science Advances, 5(9), eaaw1164. https://doi.org/10.1126/sciadv.aaw1164

Nishenko, S., & Jacob, K. (1990). Seismic potential of the queen charlotte-alaska-aleutian seismic zone. Journal of Geophysical Research, 95(B3), 2511– 2532.

Okada, Y. (1985). Surface deformation due to shear and tensile faults in a half-space. Bulletin of the seismological society of America, 75(4), 1135-1154.

Perfettini, H., Frank, W. B., Marsan, D. & Bouchon, M. (2018). A model of aftershock migration driven by afterslip. Geophys. Res. Lett. 45, 2283–2293.

Pollitz, F. F. (2014). Post-earthquake relaxation using a spectral element method: 2.5-D case. Geophysical Journal International, 198(1), 308–326. https://doi.org/10.1093/gji/ggu114

Pollitz, F. F., Bürgmann, R., & Banerjee, P. (2006). Post-seismic relaxation following the great 2004 Sumatra-Andaman earthquake on a com- pressible self-gravitating Earth. Geophysical Journal International, 167(1), 397–420. https://doi.org/10.1111/j.1365-246X.2006.03018.x

Ruppert, N. A., Rollins, C., Zhang, A., Meng, L., Holtkamp, S. G., West, M. E., & Freymueller, J. T. (2018). Complex faulting and triggered rupture during the 2018 MW 7.9 offshore Kodiak, Alaska, earthquake. Geophysical Research Letters, 45, 7533–7541. https://doi.org/10.1029/2018GL078931

Sandwell, D. T., Xu, X., Mellors, R., Wei, M., Tong, X., & Wessel, P. (2016). GMTSAR: An InSAR processing system based on generic mapping tools (2nd ed.). Retrieved from http://topex.ucsd.edu/gmtsar/tar/GMTSAR_2ND_TEX.pdf

Schwartz, S. Y. (1999). Noncharacteristic behavior and complex recurrence of large subduction zone earthquakes. Journal of Geophysical Research, 104(B10), 23111–23125. https://doi.org/10.1029/1999JB900226

Singh, S. K., & Suárez, G. (1988). Regional variation in the number of aftershocks (mb ≥ 5) of large, subduction-zone earthquakes (MW ≥ 7.0). Bulletin of the Seismological Society of America, 78, 230‑242.

Shillington, D. J., Bécel, A., Nedimović, M. R., Kuehn, H., Webb, S. C., Abers, G. A., Keranen, K. M., Li, J., Delescluse, M., & Mattei-Salicrup, G. A. (2015). Link between plate fabric, hydration and subduction zone seismicity in Alaska. Nature Geoscience, 8(12), 961– 964. https://doi.org/10.1038/ngeo2586

Shillington, D.J., B ́ecel, A., Nedimovic, M.R., 2022. Upper plate structure and megathrust properties in the Shumagin gap near the July 2020 M7.8 Simeonof event. Geophys. Res. Lett. 49 https://doi.org/10.1029/2021GL096974,32021GL096974.

Stern, R. J., Subduction zones, Rev. Geophys., 40(4), 1012, doi:10.1029/2001RG000108, 2002.

Sun, T., & Wang, K. (2015). Viscoelastic relaxation following subduction earthquakes and its effects on afterslip determination. Journal of Geophysical Research: Solid Earth, 120, 1329–1344. https://doi.org/10.1002/2014JB011707

Sun, T., Wang, K., & He, J. (2018). Crustal deformation following great subduction earthquakes controlled by earthquake size and mantle rheology. Journal of Geophysical Research: Solid Earth, 123, 5323–5345. https://doi.org/10.1029/2017JB015242

Tian, Z., Freymueller, J. T., & Yang, Z. (2021). Postseismic deformation due to the 2012 Mw 7.8 Haida Gwaii and 2013 Mw 7.5 Craig earthquakes and its implications for regional rheological structure. Journal of Geophysical Research: Solid Earth, 126, e2020JB020197. https://doi. org/10.1029/2020JB020197

Tian, Z., Freymueller, J. T., Yang, Z., Li, Z., & Sun, H. (2023). Frictional properties and rheological structure at the Ecuadorian subduction zone revealed by the postseismic deformation due to the 2016 MW 7.8 Pedernales (Ecuador) earthquake. Journal of Geophysical Research: Solid Earth, 128, e2022JB025043. https://doi. org/10.1029/2022JB025043.

United States Geological Survey National Earthquake Information Center, 2021. M 8.2–99 km S.E. of Perryville, Alaska. https://earthquake.usgs.gov/earthquakes/eventpage/ak0219neiszm/finite-fault.

Wang, K., Hu, Y., & He, J. (2012). Deformation cycles of subduction earthquakes in a viscoelastic Earth. Nature, 484(7394), 327–332. https://doi.org/10.1038/nature11032

Wang, K., & Bürgmann, R. (2020). Probing fault frictional properties during afterslip updip and downdip of the 2017 Mw 7.3 Sarpol - e Zahab earthquake with space geodesy. Journal of Geophysical Research: Solid Earth, 125, e2020JB020319. https://doi.org/10.1029/2020JB020319

Wang, K., & Fialko, Y. (2018). Observations and modeling of coseismic and postseismic deformation due to the 2015 Mw 7.8 Gorkha (Nepal) earthquake. Journal of Geophysical Research: Solid Earth, 123, 761–779. https://doi.org/10.1002/2017JB014620

Wei, S. S., Ruprecht, P., Gable, S. L., Huggins, E. G., Ruppert, N., Gao, L., & Zhang, H. (2021). Along-strike variations in intermediate-depth seismicity and arc magmatism along the Alaska Peninsula. Earth and Planetary Science Letters, 563, 116878. https://doi.org/10.1016/j.epsl.2021.116878

Wesson, R. L. (1987). Modelling aftershock migration and afterslip of the San Juan Bautista, California, earthquake of October 3, 1972. Tectonophysics 144, 215–229

Xiao, Z., Freymueller, J. T., Grapenthin, R., Elliott, J. L., Drooff, C., & Fusso, L. (2021). The deep Shumagin gap filled: Kinematic rupture model and slip budget analysis of the 2020 Mw 7.8 Simeonof earthquake constrained by GNSS, global seismic waveforms, and floating InSAR. Earth and Planetary Science Letters, 576, 117241. https://doi.org/10.1016/j.epsl.2021.117241

Yabe, S. & Ide, S. (2018). Why do aftershocks occur within the rupture area of a large earthquake? Geophys. Res. Lett. https://doi.org/10.1029/2018GL077843.

Zumberge, J. F., M. B. Heflin, D. C. Jefferson, M. M. Watkins, and F. H. Webb (1997). Precise point positioning for the efficient and robust analysis of GPS data from large networks, *Journal of Geophysical Research: Solid Earth* **102**, no. B3, 5005–5017, doi: 10.1029/96JB03860.

Zhao, B., Bürgmann, R., Wang, D., Zhang, J., Yu, J., Li, Q., 2022. Aseismic slip and recent ruptures of persistent asperities along the Alaska-Aleutian subduction zone. Nat. Commun. https://doi.org/10.1038/s41467-022-30883-7.